C. R. Mecanique 346 (2018) 1136–1152

Contents lists available at ScienceDirect

Comptes Rendus Mecanique

www.sciencedirect.com

Solid body motion prediction using a unit quaternion-based solver with actuator disk

Peng Du [a,*], Abdellatif Ouahsine [a], Yannick Hoarau [b]

[a] Laboratoire Roberval, UMR CNRS, Sorbonne Universités, Université de technologie de Compiègne, Centre de recherches Royallieu, CS 60319, 60203 Compiègne cedex, France
[b] ICUBE Laboratory, UMR 7357 CNRS, University of Strasbourg, 67000 Strasbourg, France

ARTICLE INFO

Article history:
Received 26 March 2018
Accepted 1 August 2018
Available online 27 August 2018

Keywords:
Ship hydrodynamics
Actuator disk
Open-water test
Oblique towing tank test

ABSTRACT

A six-Dof motion solver based on unit quaternions and an actuator disk model are implemented for ship hydrodynamics predictions. The six-Dof module is tested using the water entry phenomenon of a free falling sphere. The displacement history and impacting forces are analyzed. A KCS (KRISO container ship) model with the allowances of sinkage and trim is then simulated and validated. The actuator disk model is used to replace a real propeller. The open-water test of a KP458 propeller is first carried out to obtain the thrust and torque coefficients, using both the multi-run and single-run approaches. Oblique Towing Tank (OTT) tests using the actuator disk are conducted at last and the results agree well with the experiments. These models can be used for simulating six-Dof motions and captive model tests of ships.

1. Introduction

Ship hydrodynamics simulations based on CFD (Computational Fluid Dynamics) have been widely used in recent years. Potential flow theory is a great success and has provided reliable results in this area. The fluids are assumed to be inviscid and irrotational, which simplifies the original NS (Navier–Stokes) equations. Efforts have been continuously directed at directly solving the NS equations, so that more flow details can be captured. Currently, considering both the accuracy and computational cost, RANS (Reynolds-averaged Navier–Stokes)-based approaches have been adopted in many commercial and open source codes. Among them, OpenFoam is an outstanding one that provides multiple functionalities for ship simulations, including different turbulence models, mesh generation methods for complex geometries, mesh moving methods, etc. Other abilities can also be implemented for various purposes.

To simulate the six-Dof motions of a ship, a set of rigid-body equations should be solved. Two coordinate systems are normally used, an earth-fixed one and a ship-fixed one [1–3]. An important concept is the transformation between the two coordinate systems. The Euler angle-based approach has been used in many works and is intuitive to understand [1,4]. However, it fails when certain angles reach 90°. This is referred to as the gimbal lock phenomenon that limits the rigid body motions [5]. The quaternion-based method can be adopted to avoid this problem [6], which is emphasized in this work. OpenFoam uses a symplectic method originated from molecular dynamics, which rotates the rigid body a half of the Euler angle each time to avoid the gimbal lock phenomenon [7].

* Corresponding author.
E-mail addresses: pp1565156@126.com (P. Du), ouahsine@utc.fr (A. Ouahsine).

https://doi.org/10.1016/j.crme.2018.08.010

Propulsion has to be taken into account in some cases, which poses difficulties for CFD. The propeller rotation is prescribed and has to be moved with the six-Dof motions of the ship hull sometimes. Its geometry is complicated and uses a great number of meshes to capture the geometrical details. So the computational cost is greatly increased. The momentum theory can then be adopted, which is also referred to as the actuator disk model. Instead of a real propeller, it adds a volume source at a pre-defined position and the fluids there will be accelerated or rotated. Some famous methods are the vortex wake method [8], the asymptotic acceleration potential method [9], the generalized actuator disk method [10,11], etc. The body-force model proposed by Stern [12] is mostly used for propeller simulations, which has been utilized in the CFD codes of FINE-MARINE and Star-CCM+ with great success.

In this study, a six-Dof motion solver based on unit quaternions is implemented in OpenFoam. Water entry cases of a free falling sphere and a ship with free trim and sinkage are simulated. The actuator disk model is implemented for propulsion. The open-water test is first carried out to obtain the thrust and torque curves for the actuator disk. Then Oblique Towing Tank (OTT) tests are conducted for validations. These models are useful for ship hydrodynamics predictions.

2. Computational methods

2.1. Governing equations

Since DNS (Direct Numerical Simulation) and LES (Large-Eddy Simulation) are computationally expensive, the Reynolds decomposition is always used to separate the velocity fluctuations from the mean flow velocity. The Reynolds-averaged Navier–Stokes (RANS) equations can then be obtained [13]:

$$\nabla \cdot \mathbf{u} = 0 \tag{1}$$

$$\frac{\partial(\rho\mathbf{u})}{\partial t} + \nabla \cdot \big(\rho(\mathbf{u}-\mathbf{u}_g)\mathbf{u}\big) = -\nabla p^* + \nabla \cdot (\mu_{\text{eff}}\nabla\mathbf{u}) + \rho\mathbf{g} + \mathbf{f}_\sigma \tag{2}$$

where $\mathbf{u}$, ρ, p and $\mathbf{g}$ are the velocity, fluid density, pressure, and gravitation. $\mu_{\text{eff}} = \rho(\nu + \nu_t)$ is the effective dynamic viscosity. The eddy viscosity ν_t is obtained from a turbulence model. $\mathbf{f}_\sigma$ is the surface tension term. The grid velocity $\mathbf{u}_g$ is used to account for the mesh motion.

2.2. Multiphase method

The VOF (volume-of-fluid) approach is used for multiphase flow simulations, together with an artificial compression term. The transport equation reads:

$$\frac{\partial\alpha}{\partial t} + \nabla \cdot \big[\alpha(\mathbf{u}-\mathbf{u}_g)\big] + \nabla \cdot \big[\alpha(1-\alpha)\mathbf{u}_r\big] = 0 \tag{3}$$

where α is the phase fraction, which takes values within the range $0 \le \alpha \le 1$. $\alpha = 0$ and $\alpha = 1$ correspond to gas and liquid, respectively. It can be seen that the compression term (the last term on the left-hand side) only takes effect within the interface. This term is able to compress the free surface towards a sharper one. $\mathbf{u} = \alpha\mathbf{u}_w + (1-\alpha)\mathbf{u}_a$ is the effective velocity, and $\mathbf{u}_r = \mathbf{u}_w - \mathbf{u}_a$ is the relative velocity between the two phases, where the subscripts 'w' and 'a' denote water and air, respectively. The density and dynamic viscosity are calculated according to:

$$\begin{aligned} \rho &= \alpha\rho_w + (1-\alpha)\rho_a \\ \mu &= \alpha\mu_w + (1-\alpha)\mu_a \end{aligned} \tag{4}$$

The surface tension term $\mathbf{f}_\sigma$ is calculated as:

$$\mathbf{f}_\sigma = \sigma\,\kappa\,\nabla\alpha \tag{5}$$

where σ is the surface tension coefficient (0.07 kg/s^2 in water), and κ is the curvature of the free surface interface, determined from the volume of fraction by $\kappa = -\nabla \cdot (\nabla\alpha/|\nabla\alpha|)$.

2.3. 6Dof motion solver

To calculate the 6Dof motions of the ship, a set of rigid body equations should be solved, where two coordinate systems are used (Fig. 1). In the earth-fixed system, the 6Dofs of a ship, including surge, sway, heave, roll, pitch, and yaw, can be denoted as $\mathbf{u} = (\mathbf{x}_1, \mathbf{x}_2) = (x, y, z, \phi, \theta, \psi)$, where $\mathbf{x}_1$ and $\mathbf{x}_2$ are the translational and rotational motions, respectively. The linear and angular velocities are represented as $\mathbf{v} = (\mathbf{v}_1, \mathbf{v}_2) = (u, v, w, p, q, r)$. The linear velocities in the body-fixed frame can be transformed to the earth-fixed frame by:

$$\dot{\mathbf{x}}_1 = \begin{bmatrix} \dot{x} \\ \dot{y} \\ \dot{z} \end{bmatrix} = \begin{bmatrix} \cos\theta\cos\psi & \sin\phi\sin\theta\cos\psi - \cos\phi\sin\psi & \cos\phi\sin\theta\cos\psi + \sin\phi\sin\psi \\ \cos\theta\sin\psi & \sin\phi\sin\theta\sin\psi + \cos\phi\cos\psi & \cos\phi\sin\theta\sin\psi - \sin\phi\cos\psi \\ -\sin\theta & \sin\phi\cos\theta & \cos\phi\cos\theta \end{bmatrix} \begin{bmatrix} u \\ v \\ w \end{bmatrix} = \mathbf{J}_1\mathbf{v}_1 \tag{6}$$

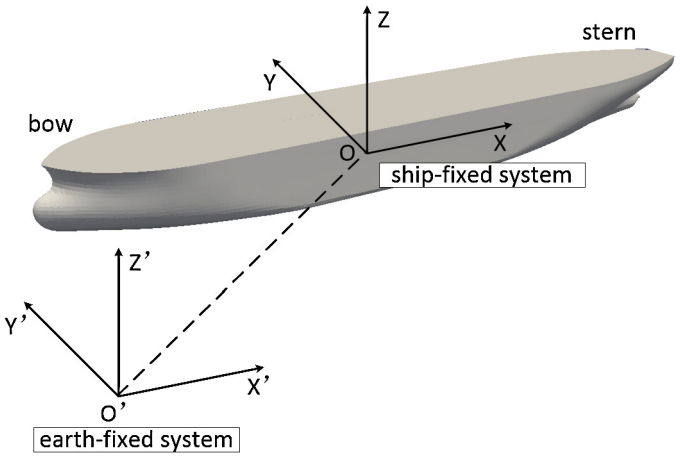

Fig. 1. Coordinate systems of the 6Dof motion solver.

The angular velocities can also be transformed as:

$$\dot{\mathbf{x}}_2 = \begin{bmatrix} \dot{\phi} \\ \dot{\theta} \\ \dot{\psi} \end{bmatrix} = \begin{bmatrix} 1 & \sin\phi\tan\theta & \cos\phi\tan\theta \\ 0 & \cos\phi & -\sin\phi \\ 0 & \sin\phi/\cos\theta & \cos\phi/\cos\theta \end{bmatrix} \begin{bmatrix} p \\ q \\ r \end{bmatrix} = \mathbf{J}_2\mathbf{v}_2 \tag{7}$$

Notice that this equation fails when $\theta = 90°$, which is known as the gimbal-lock phenomenon. To avoid the singularity problem caused by this phenomenon, another approach based on the unit quaternions is adopted. A unit quaternion is defined as a complex number with one real part η and three imaginary parts $\boldsymbol{\epsilon} = [\epsilon_1, \epsilon_2, \epsilon_3]$, which satisfies:

$$\eta^2 + \epsilon_1^2 + \epsilon_2^2 + \epsilon_3^2 = 1 \tag{8}$$

The transformation for linear and angular velocities can be realized by:

$$\dot{\mathbf{x}}_1 = \begin{bmatrix} \dot{x} \\ \dot{y} \\ \dot{z} \end{bmatrix} = \begin{bmatrix} 1-2(\epsilon_2^2+\epsilon_3^2) & 2(\epsilon_1\epsilon_2-\epsilon_3\eta) & 2(\epsilon_1\epsilon_3+\epsilon_2\eta) \\ 2(\epsilon_1\epsilon_2+\epsilon_3\eta) & 1-2(\epsilon_1^2+\epsilon_3^2) & 2(\epsilon_2\epsilon_3-\epsilon_1\eta) \\ 2(\epsilon_1\epsilon_3-\epsilon_2\eta) & 2(\epsilon_2\epsilon_3+\epsilon_1\eta) & 1-2(\epsilon_1^2+\epsilon_2^2) \end{bmatrix} \begin{bmatrix} u \\ v \\ w \end{bmatrix} = \mathbf{R}_1\mathbf{v}_1 \tag{9}$$

$$\dot{\mathbf{x}}_2 = \begin{bmatrix} \dot{\phi} \\ \dot{\theta} \\ \dot{\psi} \end{bmatrix} = \frac{1}{2} \begin{bmatrix} -\epsilon_1 & -\epsilon_2 & -\epsilon_3 \\ \eta & -\epsilon_3 & \epsilon_2 \\ \epsilon_3 & \eta & -\epsilon_1 \\ -\epsilon_2 & \epsilon_1 & \eta \end{bmatrix} \begin{bmatrix} p \\ q \\ r \end{bmatrix} = \mathbf{R}_2\mathbf{v}_2 \tag{10}$$

Quaternions and Euler angles can be translated to each other [6]. The forces and moments can be projected from the earth system into the body system in a similar way:

$$\mathbf{F} = (X, Y, Z) = \mathbf{J}_1^{-1} \cdot \mathbf{F}_e \tag{11}$$

$$\mathbf{M} = (K, M, N) = \mathbf{J}_1^{-1} \cdot \mathbf{M}_e \tag{12}$$

After calculating the forces and moments on the rigid body, the accelerations can be obtained by solving the following equations:

$$\begin{aligned}
m\left[\dot{u} - vr + wq - x_g(q^2+r^2) + y_g(pq-\dot{r}) + z_g(pr+\dot{q})\right] &= X \\
m\left[\dot{v} - wp + ur - y_g(r^2+p^2) + z_g(qr-\dot{p}) + x_g(qp+\dot{r})\right] &= Y \\
m\left[\dot{w} - uq + vp - z_g(p^2+q^2) + x_g(rp-\dot{q}) + y_g(rq+\dot{p})\right] &= Z \\
I_x\dot{p} + (I_z - I_y)qr - (\dot{r}+pq)I_{xz} + (r^2-q^2)I_{yz} + (pr-\dot{q})I_{xy} & \\
+ m\left[y_g(\dot{w} - uq + vp) - z_g(\dot{v} - wp + ur)\right] &= K \\
I_y\dot{q} + (I_x - I_z)rp - (\dot{p}+qr)I_{xy} + (p^2-r^2)I_{zx} + (qp-\dot{r})I_{yz} & \\
+ m\left[z_g(\dot{u} - vr + wq) - x_g(\dot{w} - uq + vp)\right] &= M \\
I_z\dot{r} + (I_y - I_x)pq - (\dot{q}+rp)I_{yz} + (q^2-p^2)I_{xy} + (rq-\dot{p})I_{zx} & \\
+ m\left[x_g(\dot{v} - wp + ur) - y_g(\dot{u} - vr + wq)\right] &= N
\end{aligned} \tag{13}$$

Table 1
Geometrical parameters of the KCS (KRISO container ship) model.

Parameters	Symbols	Full scale	Model scale
Scale factor	γ	1	31.599
Length between perpendiculars	L_{pp} [m]	230	7.2786
Length of waterline	L_{wl} [m]	232.5	7.3570
Maximum beam of waterline	B_{wl} [m]	32.2	1.0190
Draft	T_0 [m]	10.8	0.3418
Displacement volume	∇ [m^3]	52,030	1.6490
Block coefficient	C_{b}	0.6505	0.6505
Longitudinal center of buoyancy, fwd+	L_{cb} (%L_{pp})	−1.48	−1.48
Wetted surface area without rudder	S_{w0} [m^2]	9530	9.5441
Moment of Inertia	K_{xx}/B_{wl}	0.40	0.40
	K_{yy}/B_{wl}	0.25	0.25
	K_{zz}/B_{wl}	0.25	0.25

where $(x_{\mathrm{g}}, y_{\mathrm{g}}, z_{\mathrm{g}})$ is the vector from the center of rotation to the center of gravity. I_{xx}, I_{yy}, and I_{zz} are the moments of inertia around the center of rotation. The accelerations can then be integrated to obtain the velocities and further the ship displacements.

To diffuse the movements of the rigid body, the mesh deformation technique by solving the Laplace equation is adopted:

$$\nabla \cdot (\gamma \nabla \mathbf{u}_{\mathrm{g}}) = 0 \tag{14}$$

where γ is the diffusivity coefficient. The grid velocity $\mathbf{u}_{\mathrm{g}}$ can be obtained, and the mesh information is updated in the computational domain.

2.4. Actuator disk model

An actuator disk model is implemented to account for propulsion [12]. Instead of using a real propeller, the actuator disk accelerates and rotates the fluids passing the defined region in the axial and tangential directions. The volume forces in the two directions are expressed as:

$$\mathbf{f}_{\mathrm{b}x} = A_x r^* \sqrt{1 - r^*} \tag{15}$$

$$\mathbf{f}_{\mathrm{b}\theta} = A_\theta \frac{r^* \sqrt{1 - r^*}}{r^*(1 - r'_{\mathrm{h}}) + r'_{\mathrm{h}}} \tag{16}$$

where r is the radius of the disk, $r^* = (r' - r'_{\mathrm{h}})/(1 - r'_{\mathrm{h}})$, $r' = r/R_{\mathrm{P}}$. A_x and A_θ are computed as:

$$A_x = \frac{105}{8} \frac{T}{\pi \Delta (3R_{\mathrm{H}} + 4R_{\mathrm{P}})(R_{\mathrm{P}} - R_{\mathrm{H}})} \tag{17}$$

$$A_\theta = \frac{105}{8} \frac{Q}{\pi \Delta (R_{\mathrm{P}} - R_{\mathrm{H}})(3R_{\mathrm{P}} + 4R_{\mathrm{H}})} \tag{18}$$

R_{H} and R_{P} are the radius range of the disk. T and Q are the prescribed thrust and torque, which can be obtained from the propeller open-water test.

3. Uncertainty analysis

3.1. Mesh convergence

The mesh convergence study is conducted for a scaled KCS (KRISO container ship) model, whose geometrical parameters are shown in Table 1. Fig. 2 presents the computational domain. The regions of the free surface, bow and stern are refined to resolve the water–air interface and complex geometries. Only a half domain in the y direction is simulated by using the symmetry boundary condition at the midPlane. Detailed boundary conditions can be found in Table 2. The SST k–ω turbulence model is adopted in this case. The time derivative terms are discretized using the implicit Euler scheme. The convection term in the momentum equation is discretized with a second-order linear upwind scheme, and the convection term in the VOF equation is discretized with a second-order TVD (Total Variation Diminishing) scheme with van Leer's flux limiter. A second-order central differencing scheme with non-orthogonal correction is used for the discretization of the diffusion term. Four outer correctors are used per time step, and three pressure corrections are employed in this case. All equations are solved to the tolerance of $\mathcal{O}(-8)$.

Three types of grids are designed in Table 3. The mesh is generated using the snappyhexMesh utility in OpenFoam. A background mesh is first generated and then the meshes at the target geometry are split and snapped. Boundary layer

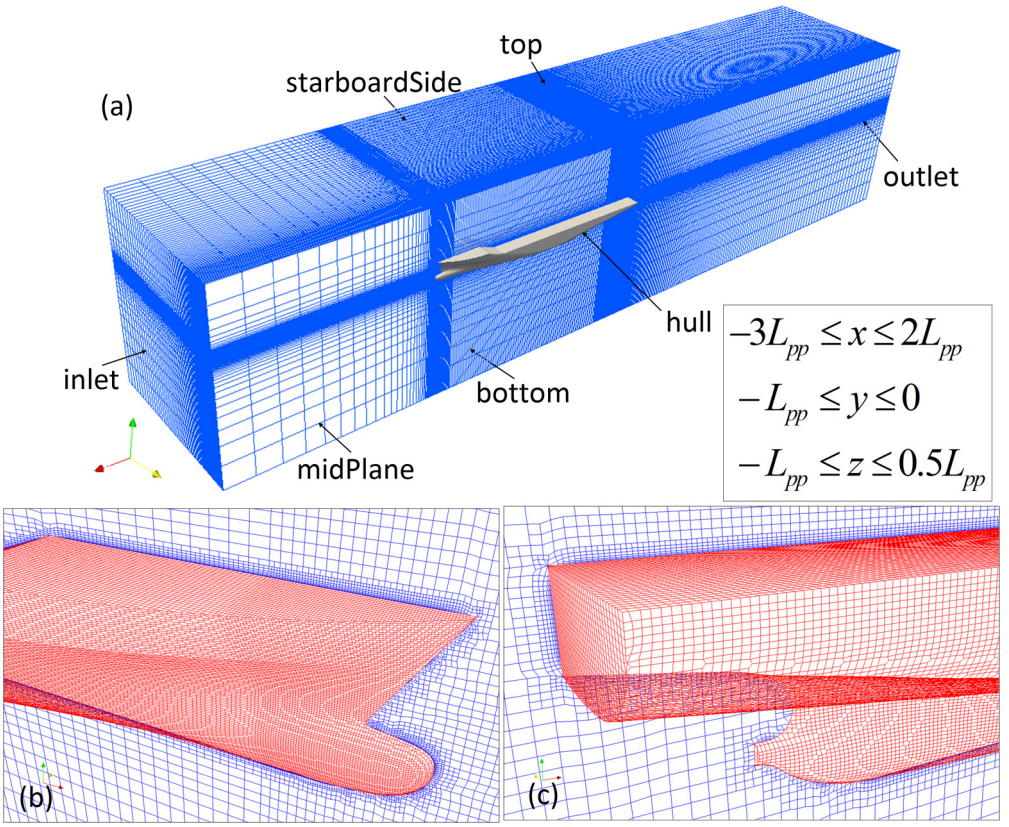

Fig. 2. Computational domain (a) of the KCS model and the mesh near (b) the bow and (c) the stern.

Table 2
Boundary conditions of the mesh convergence study.

	U	*p_rgh*	*alpha.water*
inlet	fixedValue	fixedFluxPressure	fixedValue
outlet	inletOutlet	zeroGradient	inletOutlet
top	pressureInletOutletVelocity	totalPressure	inleOutlet
hull	movingWallVelocity	fixedFluxPressure	zeroGradient
midPlane	symmetry	–	–
starboardSide	symmetry	–	–
bottom	symmetry	–	–

	k	*nut*	*omega*
inlet	fixedValue	fixedValue	fixedValue
outlet	inletOutlet	zeroGradient	inletOutlet
top	inletOutlet	zeroGradient	inletOutlet
hull	kqRWallFunction	nutkWallFunction	omegaWallFunction
midPlane	symmetry	–	–
starboardSide	symmetry	–	–
bottom	symmetry	–	–

meshes are added at last, which are controlled to make the non-dimensional wall distance in the range $30 < y^+ < 200$. A refinement ratio $\sqrt{2}$ is used for the background mesh, as suggested by the ITTC (International Towing Tank Conference) [14]. Since the mesh near the hull is refined to a certain level based on the background mesh, the final mesh ratio is larger than $\sqrt{2}$ in Table 3. The ship is fixed in the domain, and a constant velocity (2.196 m/s) is added at the inlet for the fluids. The corresponding Froude (Fr) and Reynolds numbers (Re) are 0.26 and 1.4×10^7. The grid convergence of the total resistance coefficient is analyzed.

The convergence ratio (R_C) and order of accuracy (p_C) can be calculated according to:

$$R_C = \frac{\epsilon_C^{21}}{\epsilon_C^{32}} \tag{19}$$

Table 3
Grid convergence results of the total resistance coefficient.

Parameters	Values
Grid 1; 2; 3	4,032,156; 1,706,703; 712,650
r	$\sqrt{2}$
C_T^{exp} ($\times 10^{-3}$)	3.56
C_T^1 ($\times 10^{-3}$)	3.554
C_T^2 ($\times 10^{-3}$)	3.539
C_T^3 ($\times 10^{-3}$)	3.513
R_C	0.600
p_C	1.473
C_{ext}^{21} ($\times 10^{-3}$)	3.579
e_a^{21} (%)	0.447
e_{ext}^{21} (%)	0.666
GCI_{fine}^{21} (%)	1.348

Table 4
Comparison of the frictional and pressure coefficients in the mesh convergence cases. The frictional coefficient is estimated by the ITTC 1957 friction line $C_F = 0.075/(\log_{10} Re - 2)^2$. $C_P = C_T - C_F$.

Parameters	ITTC 1957	Grid 1	Grid 2	Grid 3
C_F ($\times 10^{-3}$)	2.832	2.822	2.810	2.789
C_P ($\times 10^{-4}$)	7.28	7.32	7.29	7.24

$$p_C = \frac{\ln(|\epsilon_C^{32}/\epsilon_C^{21}|)}{\ln(r)} \tag{20}$$

where $\epsilon_C^{21} = C_T^2 - C_T^1$ and $\epsilon_C^{32} = C_T^3 - C_T^2$ are the change of resistance coefficients (C_T). The subscripts 1, 2 and 3 denote the fine, medium, and coarse meshes. The experimental results related to the total resistance coefficient (C_T^{exp}) are also listed in Table 3 for comparison; they are close to the simulation results. The frictional and pressure resistance coefficients are also calculated and compared with the ITTC 1957 friction line in Table 4. Three possible conditions can be diagnosed:

- $0 < R_C < 1$ monotonic convergence;
- $R_C < 0$ oscillatory convergence;
- $R_C > 1$ divergence.

Hence the simulations in this study are monotonically convergent. The Richardson extrapolation is adopted to define the extrapolated resistance coefficient (C_{ext}^{21}), approximate relative error (e_a^{21}), extrapolated relative error (e_{ext}^{21}) and fine-grid convergence index (GCI_{fine}^{21}). The numerical uncertainty for the total resistance in this work is 1.348%.

$$C_{ext}^{21} = \frac{r^{p_C} C_T^1 - C_T^2}{r^{p_C} - 1} \tag{21}$$

$$e_a^{21} = \left| \frac{C_T^1 - C_T^2}{C_T^1} \right| \tag{22}$$

$$e_{ext}^{21} = \left| \frac{C_{ext}^{21} - C_T^1}{C_{ext}^{21}} \right| \tag{23}$$

$$GCI_{fine}^{21} = \frac{1.25 e_a^{21}}{r^{p_C} - 1} \tag{24}$$

Fig. 3 shows the wave elevation contours in the three cases. The waves are resolved better with a finer mesh. Considering both the accuracy and the simulation time, the mesh generation strategy 2 is used for the following studies. The wave profiles of case 2 agree well with the experiments in Fig. 4.

3.2. Time-step convergence

The time convergence study is carried out for the KVLCC2 model (Table 5). The computational domain and the meshes near the bow and stern can be found in Fig. 5, with the total cell number 818,372. The boundary conditions, the numerical schemes, and the convergence criterion are the same as in Section 3.1. The SST k–ω model is used in this case.

As in Fig. 6, four time steps are designed. Because of the use of the PIMPLE (merged PISO-SIMPLE) scheme, large time steps can be adopted. The maximum Courant number in this study reaches 60 and the case is still convergent. Twenty

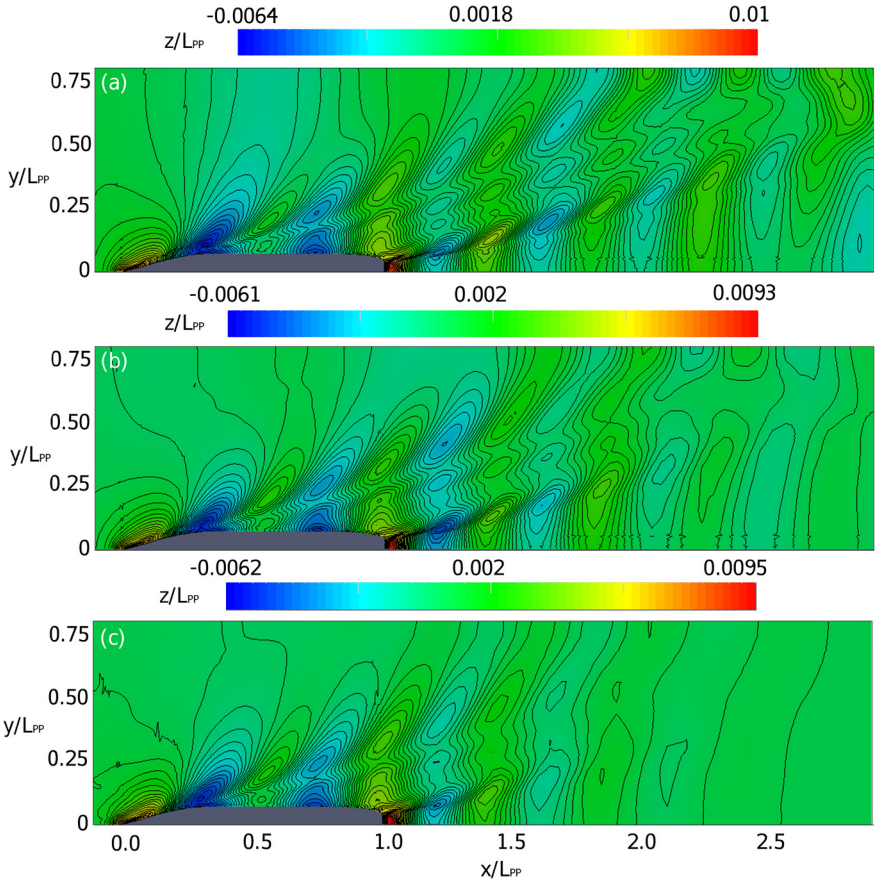

Fig. 3. Wave elevation contours of (a) grid 1; (b) grid 2; (c) grid 3.

processors are used for this case. It can be seen that the simulation times are greatly reduced. The results of the four cases seem all reasonable. The frictional and pressure resistances are also calculated and compared with the ITTC 1957 friction lines in Table 6. However, the accuracy of case 4 ($\Delta t = 1 \times 10^{-1}$ s) is clearly not enough. Although the trend is correct, large fluctuations can be found in the convergence history and the wave profiles. A very small time step ($\Delta t = 1 \times 10^{-4}$ s) can capture small changes during convergence, but the simulation time is enormously increased. As a compromise, time steps 10^{-2} and 10^{-3} s are preferred in this work. Steady solutions are sought in this case. Another transient case with different time steps are also studied in the following section.

4. Numerical results and discussions

4.1. Water entry of a free falling sphere

The water-entry phenomenon of a free falling sphere is first simulated to validate the six-Dof motion solver. The computational domain can be found in Fig. 7, with the sphere placed 1 m above the free surface. The density of the sphere is 500 kg/m^3 (half of the water density). The total grid number is 665,409. The numerical schemes are the same as in Section 3.1. Six outer correctors and four pressure correctors are used since transient behaviors are important in this case, with five different time steps 1×10^{-2}, 5×10^{-3}, 1×10^{-3}, 5×10^{-4}, 1×10^{-4} s. The boundary conditions are shown in Table 7. No turbulence model is adopted in this case. Since no wave absorption techniques are used, the boundaries are placed far from the sphere, and the mesh size is incremented from the sphere so that waves can be diffused.

The displacement and vertical force histories are compared with [18] (Figs. 8–9). The overall results agree with the work of [18]. The converge histories of the displacement and vertical force for the time steps 1×10^{-3}, 5×10^{-4} and 1×10^{-4} are close. The impact forces when the sphere first touches the free surface are predicted as close to those in the work of Shen [18]. Discrepancies can be seen after about 4 s, where our results diffuse more. This may be caused by the fact that Shen and Wan [18] used sponge layers around the sphere, which would suffer less influence from wave reflections. Although the mesh used here is designed specifically to reduce this phenomenon, the waves cannot be fully diffused by this method. However, both works converge to the same values at last. Small time steps ($\leq 1 \times 10^{-3}$ in this case) are better to be used for transient simulations.

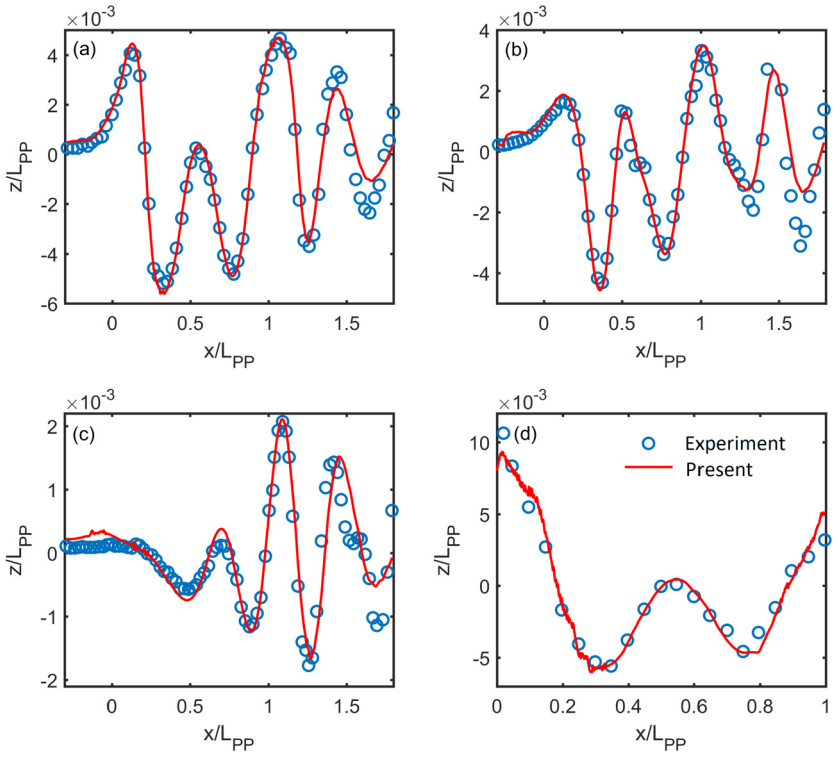

Fig. 4. Wave profiles of case 2 at three lateral positions (a) $y/L_{pp} = 0.0741$; (b) $y/L_{pp} = 0.1509$; (c) $y/L_{pp} = 0.4224$ and (d) on the hull surface [15].

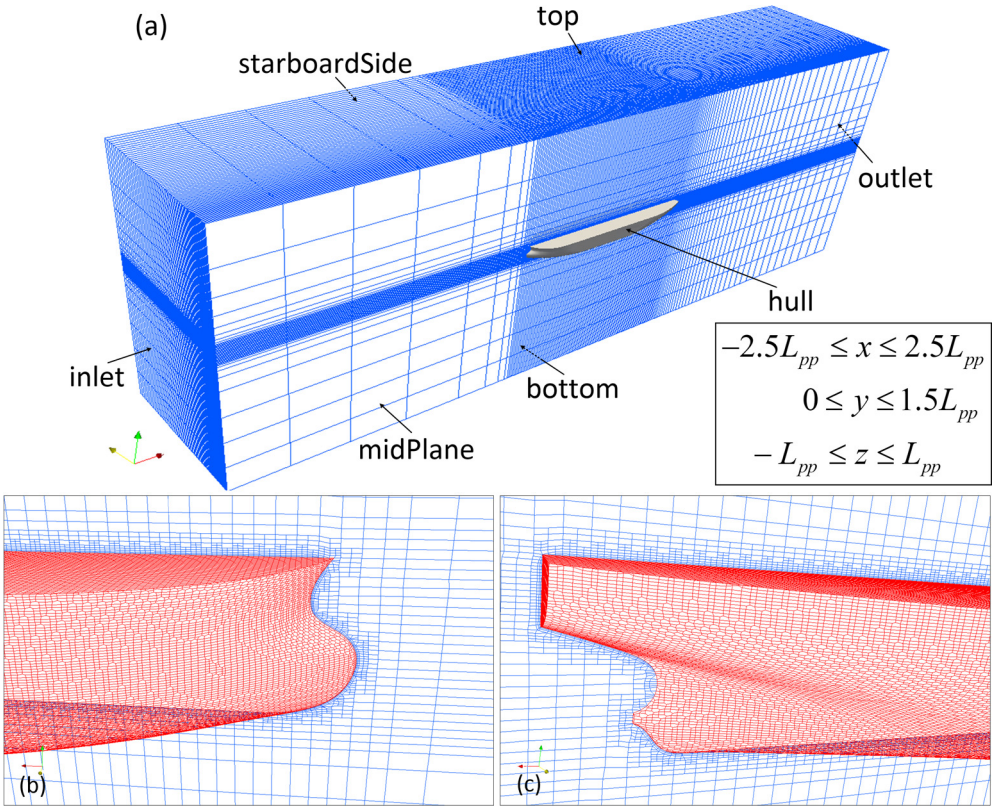

Fig. 5. Computational domain (a) of the KVLCC2 model and the mesh near (b) the bow and (c) the stern.

Table 5
Geometrical parameters of the KVLCC2 model.

Parameters	Symbols	Full scale	Model scale
Scale factor	γ	1	58
Length between perpendiculars	L_{pp} [m]	320	5.5172
Length of waterline	L_{wl} [m]	325.5	5.6121
Maximum beam of waterline	B_{wl} [m]	58	1.0000
Draft	T_0 [m]	20.8	0.3586
Displacement volume	∇ [m^3]	312,622	1.6023
Block coefficient	C_b	0.8098	0.8098
Longitudinal center of buoyancy, fwd+	L_{cb} (%L_{pp})	3.48	3.48
Wetted surface area without rudder	S_{w0} [m^2]	27194	8.0838
Moment of inertia	K_{xx}/B_{wl}	0.40	0.40
	K_{yy}/B_{wl}	0.25	0.25
	K_{zz}/B_{wl}	0.25	0.25

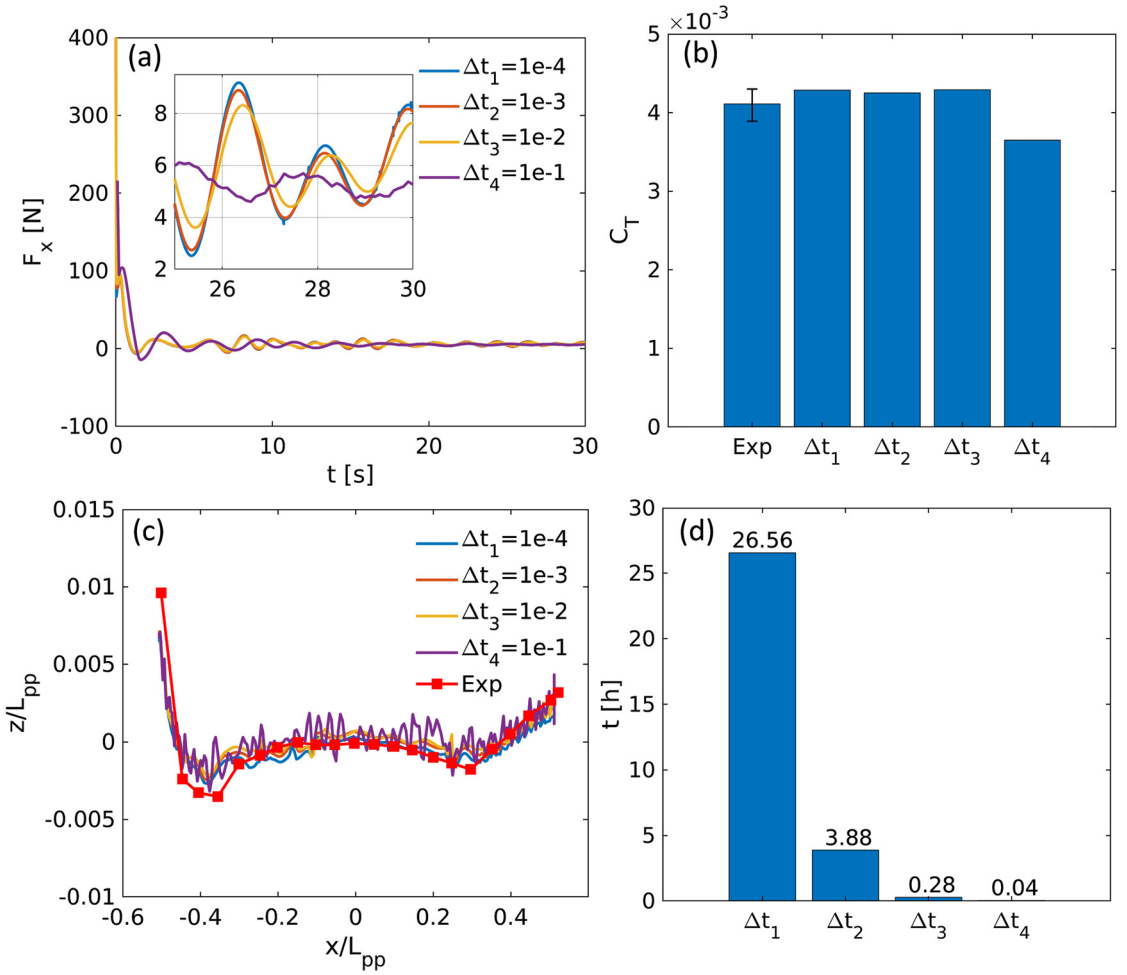

Fig. 6. Convergence history of (a) the drag, (b) total resistance coefficients, (c) wave profiles on the hull and (d) simulation time with different time steps [16]. The reported experimental uncertainty is 1% [17].

Table 6
Comparison of the frictional and pressure coefficients of the time step convergence cases. The frictional coefficient is estimated by the ITTC 1957 friction line $C_F = 0.075/(\log_{10} Re - 2)^2$. $C_P = C_T - C_F$.

Parameters	ITTC 1957	Δt_1	Δt_2	Δt_3	Δt_4
C_F ($\times 10^{-3}$)	3.453	3.315	3.313	3.340	2.101
C_P ($\times 10^{-3}$)	0.657	0.973	0.935	0.951	1.550

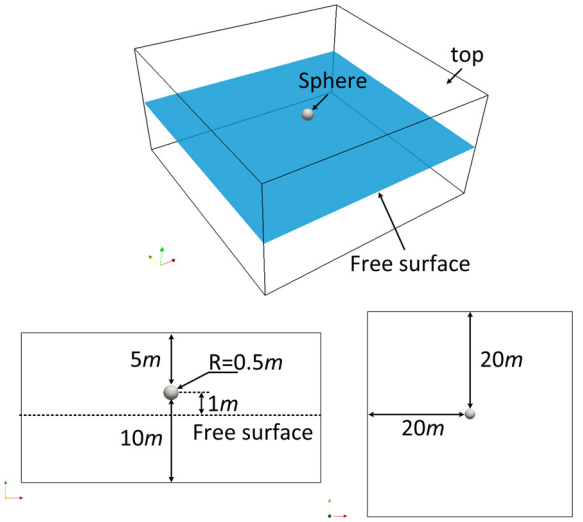

Fig. 7. Computational domain of the water entry case.

Table 7
Boundary conditions of the water entry case.

	U	*p_rgh*	*alpha.water*
top	zeroGradient	fixedValue	inletOutlet
sphere	movingWallVelocity	zeroGradient	zeroGradient
others	fixedValue	zeroGradient	zeroGradient

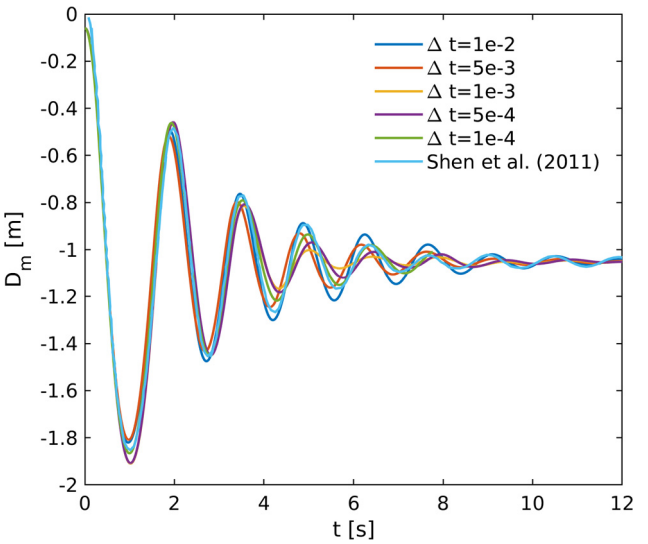

Fig. 8. Comparison of the displacement history of the free falling sphere [18].

4.2. Trim and sinkage prediction

A KCS model (Table 1) with free sinkage and trim is simulated in this case. The case setups are shown in Table 8, where six different ship velocities are designed. The boundary conditions are shown in Table 2. The SST k–ω model is used in this case. The grid number is 1,074,514. The numerical schemes, corrector numbers, and convergence criterion are the same as in the water entry case. The resistance coefficient (C_T), sinkage (σ) and trim (τ) are calculated and compared with experiments [19]. The resistance coefficient is calculated as:

$$C_T = \frac{X_T}{\frac{1}{2}\rho U_{in}^2 S_{w0}} \tag{25}$$

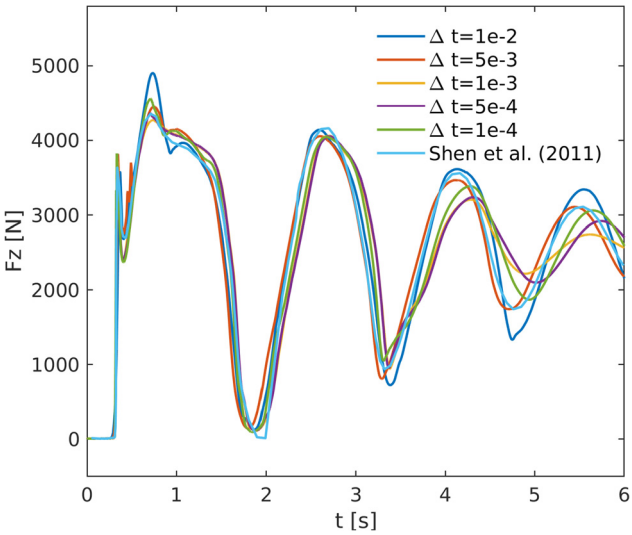

Fig. 9. Comparison of the vertical force history of the free falling sphere [18].

Table 8
Case setups of the trim and sinkage prediction for the KCS model.

Case No.	1	2	3	4	5	6
U_{in} [m/s]	0.914	1.281	1.647	1.922	2.196	2.380
Fr	0.108	0.152	0.195	0.227	0.260	0.282
Re	6.66×10^6	9.32×10^6	1.20×10^7	1.40×10^7	1.60×10^7	1.73×10^7

where X_{T}, U_{in}, and S_{w0} are the total resistance, the ship speed, and the wetted surface area at rest. In Fig. 10, the resistance coefficients are underestimated for $Fr \leq 0.260$. The sinkage is underestimated for $Fr \leq 0.195$ and overestimated for $Fr \geq 0.260$. The trim prediction is fairly well, with only the case $Fr = 0.108$ underestimated and $Fr = 0.282$ overestimated. The largest error of the three parameters are about 3.0%, 6.4% and 7.1% respectively. Overall, the implemented six-Dof model can predict the ship resistance and motion states with satisfactory accuracy.

Low-speed cases are comparably more difficult to predict, since the change of the ship-generated waves is smaller. Finer meshes at the free surface are needed. This can be observed in Fig. 11, where the wave elevations on the hull surface are extracted and compared. The wave elevations at the bow and stern rise with the increase of the ship speed. The waves at the middle of the ship are more obvious with a higher speed, and the wave height is also larger. Therefore, special attention should be paid to high speed since the ship will have large motion changes, which increase the difficulty for ship maneuvering.

4.3. Open-water test of a propeller

The open-water test of a KP458 propeller is carried out to obtain the curves of the thrust and torque coefficients, which are useful to determine the thrust and torque values for the actuator disk model. The geometrical parameters of the propeller can be found in Table 9.

The computational domain is designed as in Fig. 12. The domain extends five propeller diameters (D) upstream, 10 diameters downstream, and 10 diameters in the lateral direction. The region near the propeller is refined to capture the flow details. The boundary conditions are shown in Table 10. The SST k–ω model is adopted in this case. The grid number and time step are 1,089,926 and 1×10^{-3} s, respectively. The outer correctors and pressure correctors are 18 and 3. All the domain rotates with a prescribed rotation velocity. The inlet velocity (U_{in}) is varied to obtain different advance coefficient (J):

$$J = \frac{U_{\text{in}}}{n\,D} \tag{26}$$

Two methods are used during the open-water tests, the single-run approach and multi-run approach [20]. The multi-run approach is the normal one where a constant inlet velocity is used. The single-run approach ramps up the inlet velocity with a small acceleration such that the time derivatives become negligible, thus the solution is in a quasi-steady state. The obtained result covers a wide range in a single run, which is time-saving. After the simulations, the thrust (T) and torque (Q) can be measured, the corresponding coefficients can be calculated as:

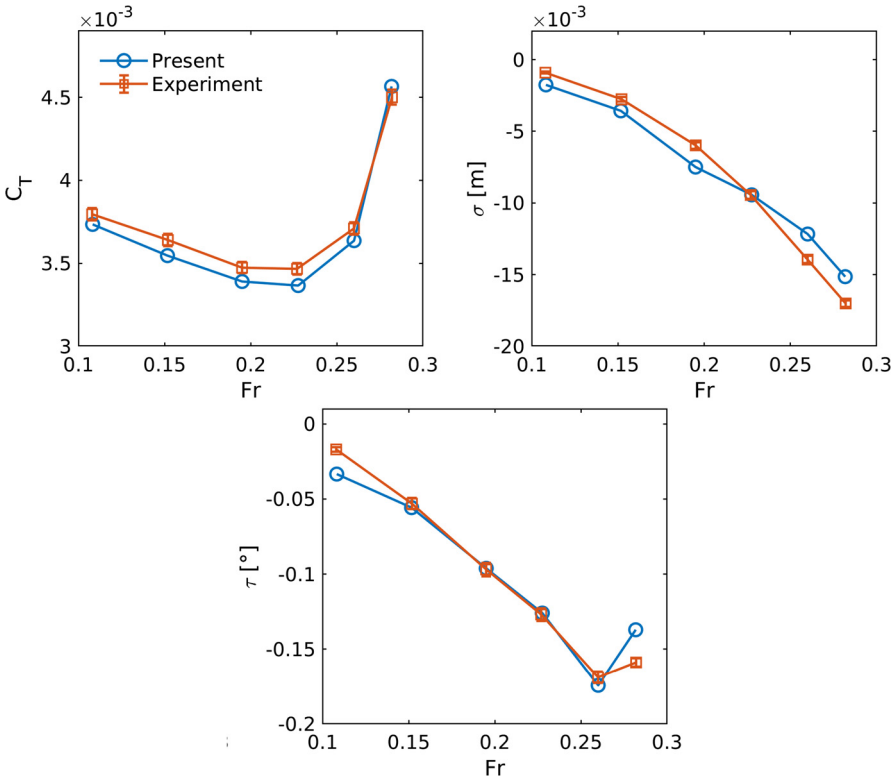

Fig. 10. Comparison of resistance coefficient (C_T), sinkage (σ) and trim (τ) with experimental data [19].

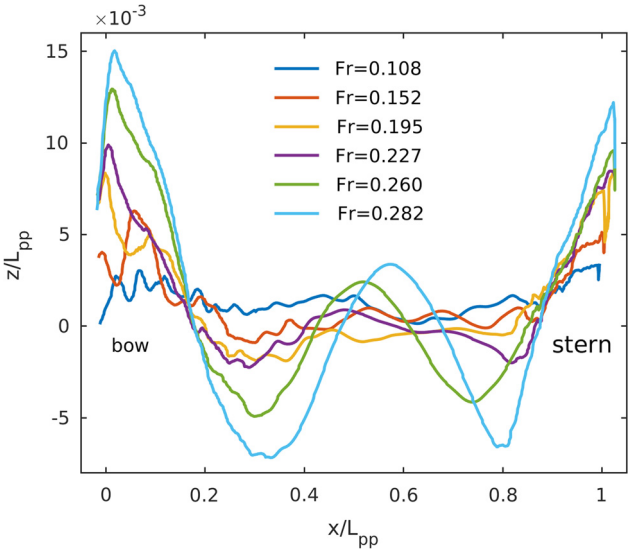

Fig. 11. Wave elevations on the hull surface with different Froude numbers (Fr).

$$K_T = \frac{T}{\rho n^2 D^4} \quad K_Q = \frac{Q}{\rho n^2 D^5} \tag{27}$$

The simulation results can be found in Fig. 13. Both approaches agree with experiments, except for the beginning of the single-run approach. This is because the initial parameters may not be realistic and the flows could evolve with the simulation. The values out of the experimental range ($J > 0.8$) are also predicted well. The vortical structures of $Q_V = 300\ s^{-2}$, the second invariant of the velocity gradient tensor, with different advance coefficients are shown in Fig. 14. The tip vortexes are resolved well. However, because of RANS, detailed vortical structures as in [21] are not captured. This is a trade-off between the flow details, accuracy, and computational costs.

Table 9
Geometrical parameters of the KP458 propeller.

Parameters	Symbols	Values
No. of blades	n_b	4
Diameter	D [m]	0.090
Pitch ratio	P/D	0.721
Area ratio	A_e/A_0	0.431
Hub ratio	d_h/D	0.155
Rotation		Right hand

Table 10
Boundary conditions of the open-water test.

	U	*p*	*k*	*nut*	*omega*
Inlet	fixedValue	zeroGradient	fixedValue	calculated	fixedValue
Outlet	inletOutlet	fixedValue	inletOutlet	calculated	inletOutlet
Propeller	movingWallVelocity	zeroGradient	kqRWallFunction	nutkWallFunction	omegaWallFunction

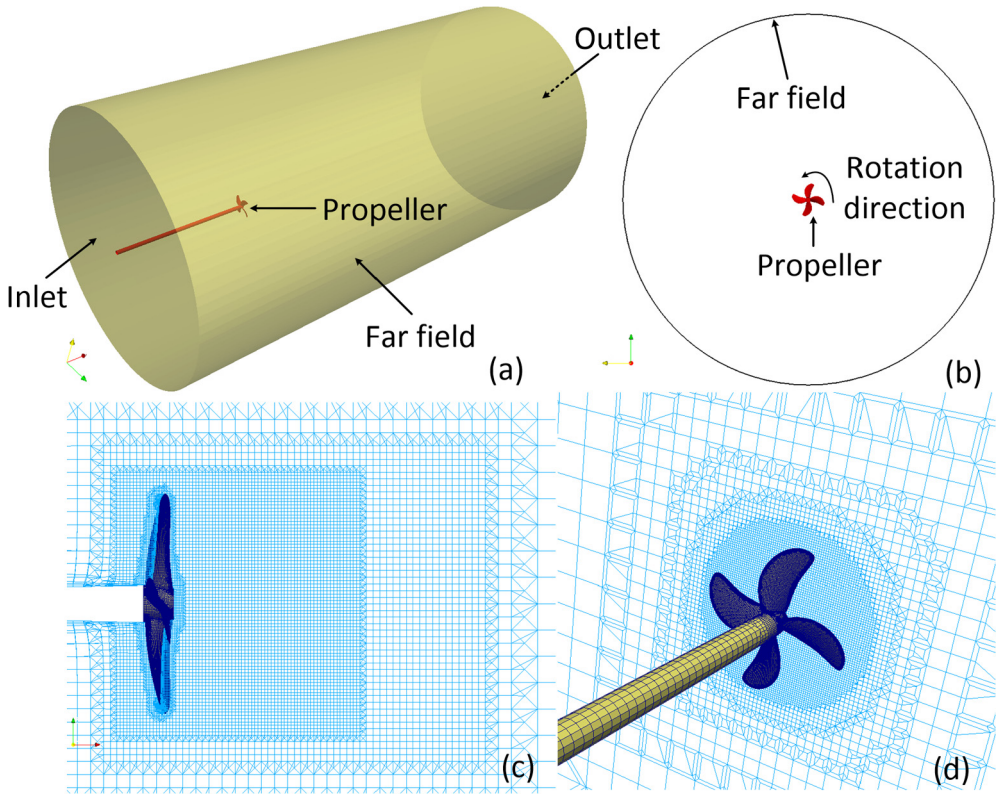

Fig. 12. Computational domain and mesh for the open-water test.

4.4. Oblique towing tank test

Oblique towing tank (OTT) tests are carried out for the KVLCC2 ship (Table 5) with the actuator disk. The computational domain is designed as in Fig. 15. The boundary conditions are the same as in Table 2 without 'midPlane' and 'starboardSide'. The SST k–ω model is adopted in this case. The cell number is 2,361,223. The numerical schemes and convergence criterion are the same as in Section 3.1. During the simulations, the same mesh is used while the inlet velocities are changed to realize different oblique conditions. This avoids remeshing when changing the drift angle of the ship. The actuator disk is located as the real propeller (Table 9). The case setups are shown in Table 11. Five drift angles are designed in this study. The inlet velocity and revolution rate of the KP458 propeller are 0.76 m/s and 17.95 rps. The thrust values are taken from [22], which are used to determine the torque according to the open-water test result (Fig. 13).

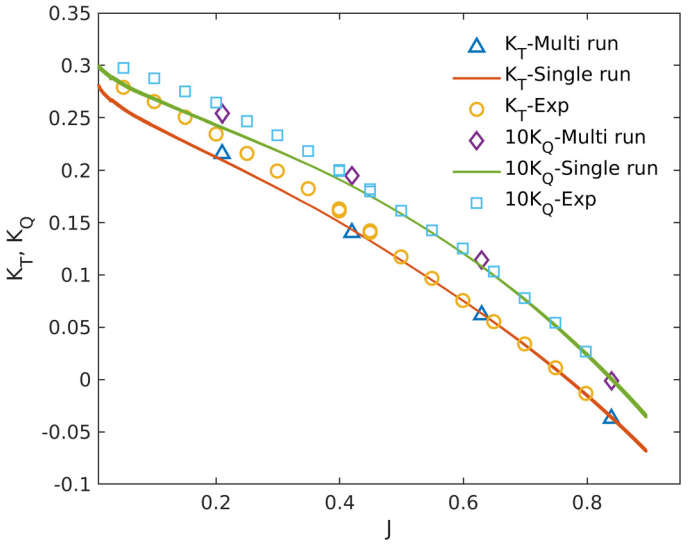

Fig. 13. Open-water test results for the KP458 propeller.

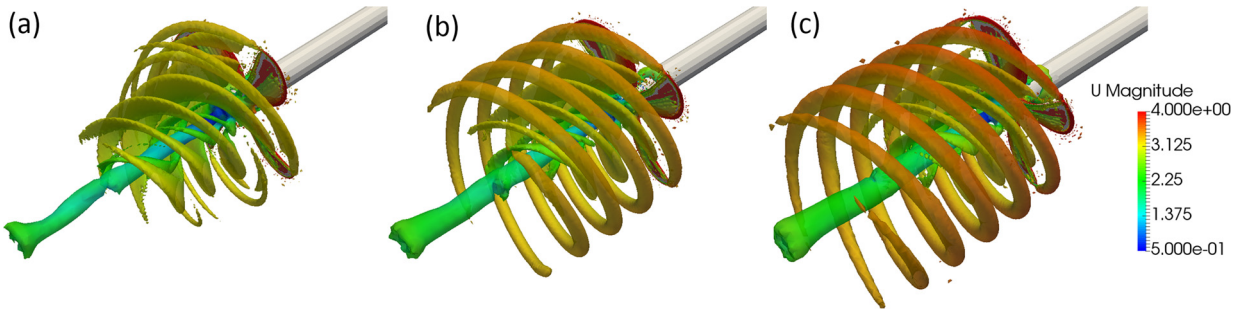

Fig. 14. Vortexes ($Q_v = 300\ s^{-2}$) generated by the propeller with different advance coefficients: (a) $J = 0.8$; (b) $J = 0.85$; (c) $J = 0.9$.

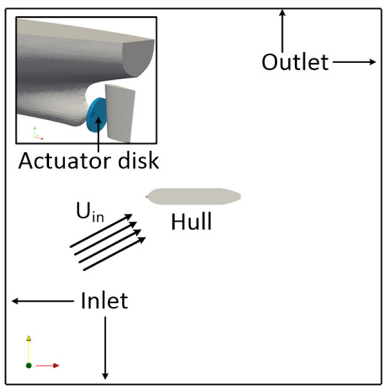

Fig. 15. Computational domain and boundary conditions of the Oblique Towing Tank (OTT) test.

Table 11
Setups of the Oblique Towing Tank (OTT) tests.

Parameters	Symbols	Values
Inlet velocity	U_{in} [m/s]	0.76
Ship drift angle	β [°]	4, 8, 12, 16, 20
Thrust	T [N]	4.321, 3.810, 4.054, 3.735, 3.784
Torque	Q [N m]	0.0872, 0.0822, 0.0845, 0.0815, 0.0820

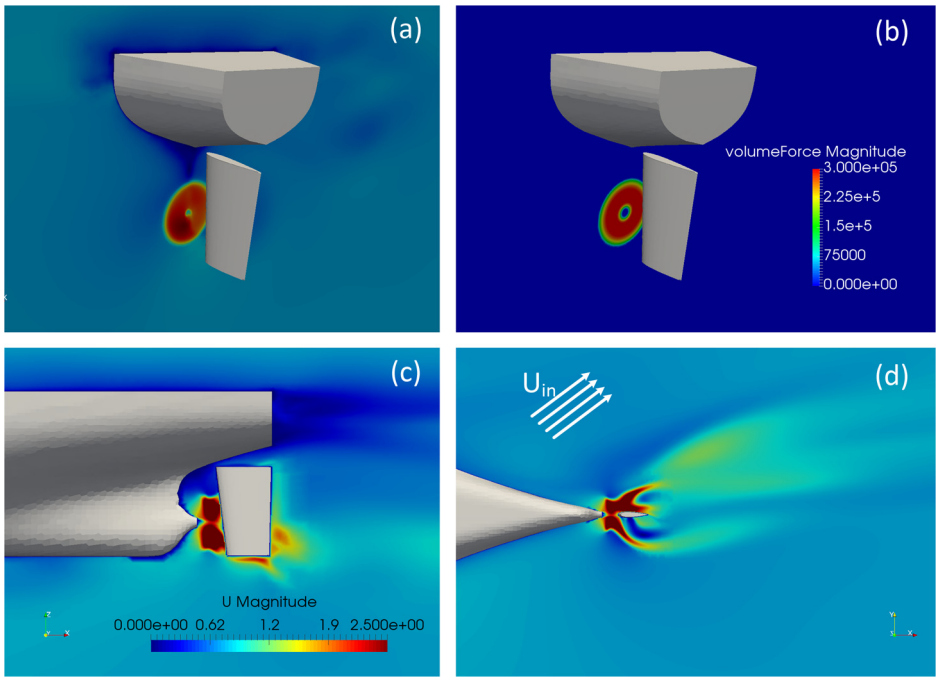

Fig. 16. Velocity contours (a, c, d) and volume force (b) at the actuator disk position ($\beta = 20°$).

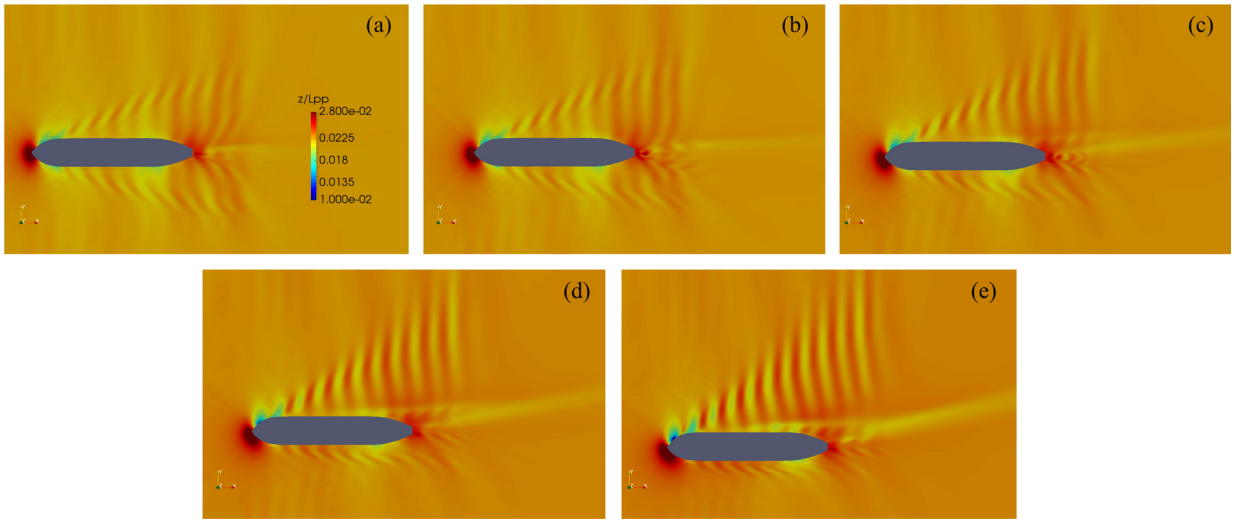

Fig. 17. Ship-generated waves with different drift angles (β) of the Oblique Towing Tank (OTT) tests. (a) $\beta = 4°$; (b) $\beta = 8°$; (c) $\beta = 12°$; (d) $\beta = 16°$; (e) $\beta = 20°$.

The case with the drift angle $\beta = 20°$ is presented in Fig. 16. The volume force created by the actuator disk can be clearly observed at the prescribed position. The velocity field there is also changed since the passed fluids are accelerated and rotated. Because of the oblique condition, the flow is forced to the starboard side.

The ship-generated waves are shown in Fig. 17. The flow fields are obviously redistributed by the oblique inlet velocities. Because of the actuator disk, the wave elevations behind the stern are influenced. The waves at the starboard side propagate further by the oblique velocity.

The wave profiles on the starboard and port sides of the hull surface are extracted in Fig. 18. On the port side, the wave is lower with a smaller drift angle. This is because when the drift angle is large, the flow will interact directly with the port side and climb up the hull surface. On the starboard side, the wave elevation is larger when the drift angle is smaller. The differences mainly lie near the bow.

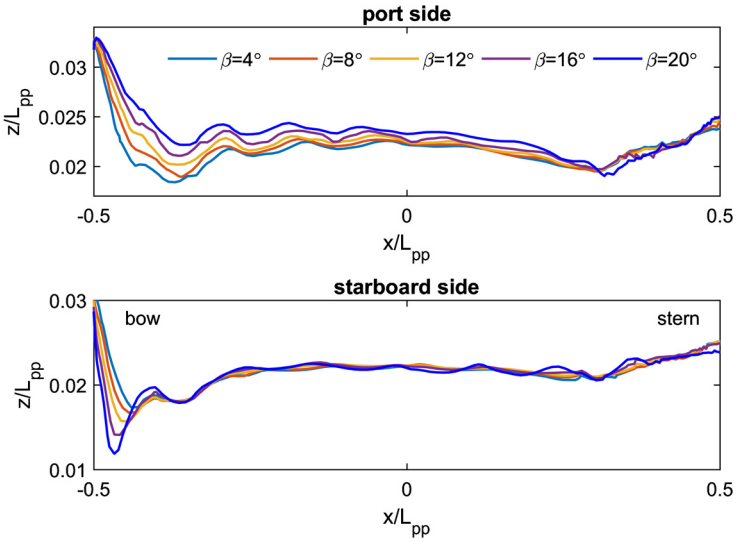

Fig. 18. Comparison of ship waves on the hull with different drift angles at the starboard and port sides.

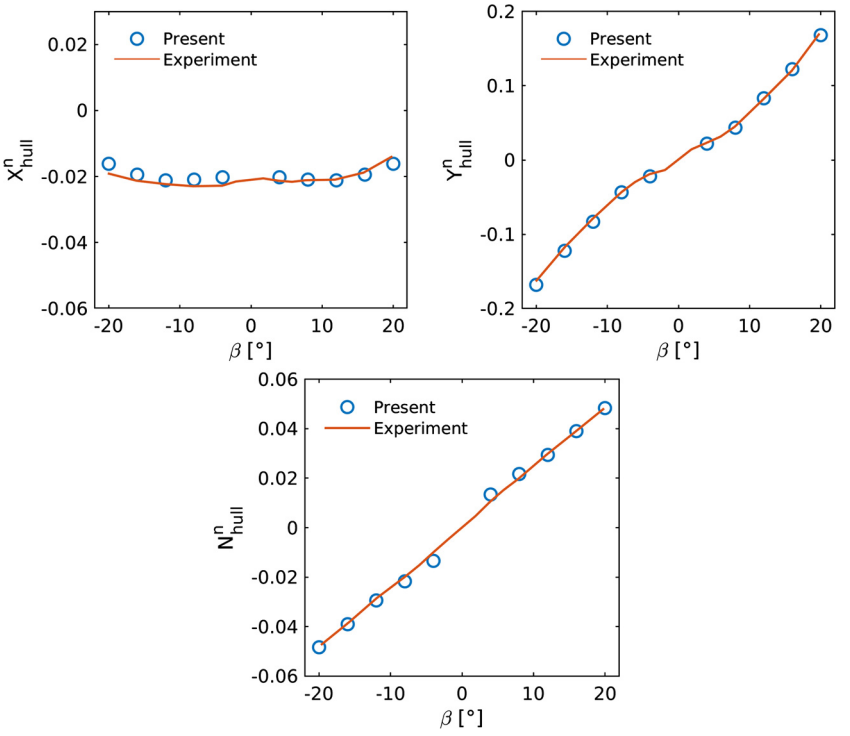

Fig. 19. Non-dimensional forces and moment of the Oblique Towing Tank (OTT) tests.

The forces and moment on the hull are extracted in Fig. 19, which are non-dimensionalized according to:

$$X^n_{\text{hull}} = \frac{X_{\text{hull}}}{\frac{1}{2}\rho L_{\text{pp}} T_{\text{d}} U^2_{\text{in}}} \quad Y^n_{\text{hull}} = \frac{Y_{\text{hull}}}{\frac{1}{2}\rho L_{\text{pp}} T_{\text{d}} U^2_{\text{in}}} \quad N^n_{\text{hull}} = \frac{N_{\text{hull}}}{\frac{1}{2}\rho L^2_{\text{pp}} T_{\text{d}} U^2_{\text{in}}} \tag{28}$$

where X_{hull}, Y_{hull} and N_{hull} are the longitudinal, lateral forces and moment on the hull. T_{d} is the ship draft. The non-dimensional forces and moment agree well with the experimental results [22]. Only the simulations with positive drift angles were carried out. The negative drift angle part is projected directly from the positive ones (Fig. 19). The ship has larger lateral force and yawing moment with a larger drift angle. These results are useful for calculating the hydrodynamic coefficients in system-based maneuvering simulations.

5. Conclusions

A six-Dof motion solver with an actuator disk model is implemented into the open source code OpenFoam. The six-Dof motion solver is based on unit quaternions, which can avoid the gimbal lock phenomenon limiting the rigid body motions. A water entry problem of a free falling sphere and a KCS model with six different ship velocities are used for validating the performance of the six-Dof motion solver. For the water entry case, the displacement and vertical force on the sphere are analyzed and compared with former researches. For the KCS case, the resistance coefficient, sinkage, and trim are validated using experimental data. The wave elevations on the hull surface are analyzed for different ship speeds. The ship hydrodynamics is harder to predict when the speed is low.

The open-water test of a KP458 propeller is simulated to obtain the torque and thrust coefficients as functions of the advance coefficient. Both the multi-run and single-run approaches are used and compared with experiments. The obtained curves are used to calculate the torque and thrust values for the actuator disk model. In the OTT tests, five different drift angles with the actuator disk are designed. The volume forces generated by the actuator disk changes the flow fields and create similar effects as a real propeller, with less computational mesh and duration. The analyses of the ship-generated waves and forces/moment on the hull prove the validity of our model. These models can be used for six-Dof motion simulations and captive model tests of ships.

Acknowledgements

The computations in this paper were performed on the HPC cluster of the University of Strasbourg and the cluster "TENSOR" of the University of Technology of Compiègne (UTC), France. The first author acknowledges the financial support by the China Scholarship Council (CSC).

References

[1] P.M. Carrica, R.V. Wilson, R.W. Noack, F. Stern, Ship motions using single-phase level set with dynamic overset grids, Comput. Fluids 36 (9) (2007) 1415–1433.
[2] P. Du, A. Ouahsine, K. Toan, P. Sergent, Simulation of ship maneuvering in a confined waterway using a nonlinear model based on optimization techniques, Ocean Eng. 142 (2017) 194–203.
[3] P. Du, A. Ouahsine, P. Sergent, Influences of the separation distance, ship speed and channel dimension on ship maneuverability in a confined waterway, C. R. Mecanique 346 (5) (2018) 390–401.
[4] Z. Shen, D. Wan, P.M. Carrica, Dynamic overset grids in openfoam with application to kcs self-propulsion and maneuvering, Ocean Eng. 108 (2015) 287–306.
[5] V. Vukčević, H. Jasak, I. Gatin, Implementation of the ghost fluid method for free surface flows in polyhedral finite volume framework, Comput. Fluids 153 (2017) 1–19.
[6] T.I. Fossen, Handbook of Marine Craft Hydrodynamics and Motion Control, John Wiley & Sons, 2011.
[7] A. Dullweber, B. Leimkuhler, R. McLachlan, Symplectic splitting methods for rigid body molecular dynamics, J. Chem. Phys. 107 (15) (1997) 5840–5851.
[8] R. Miller, The aerodynamics and dynamic analysis of horizontal axis wind turbines, in: Wind Engineering 1983, Part 3C, Elsevier, 1984, pp. 329–340.
[9] G.J.W. Van Bussel, The Aerodynamics of Horizontal Axis Wind Turbine Rotors Explored with Asymptotic Expansion Methods, Ph.D. thesis, Delft University of Technology, Delft, The Netherlands, 1995.
[10] J.T. Conway, Analytical solutions for the actuator disk with variable radial distribution of load, J. Fluid Mech. 297 (1995) 327–355.
[11] J.N. Sørensen, A. Myken, Unsteady actuator disc model for horizontal axis wind turbines, J. Wind Eng. Ind. Aerodyn. 39 (1992) 139–149.
[12] F. Stern, H. Kim, V. Patel, A viscous-flow approach to the computation of propeller–hull interaction, J. Ship Res. 32 (4) (1988) 246–262.
[13] P. Du, A. Ouahsine, P. Sergent, Hydrodynamics prediction of a ship in static and dynamic states, Coupled Syst. Mech. 7 (2) (2018) 163–176.
[14] ITTC, Recommended procedures and guidelines: uncertainty analysis in CFD verification and validation methodology and procedures, in: Proceedings of the 25th International Towing Tank Conference, Fukuoka, Japan, 14–20 September 2008.
[15] T. Hino, Proceedings of CFD Workshop, Tokyo, Japan, 2005, 2005.
[16] F. Pereira, L. Eça, G. Vaz, Verification and validation exercises for the flow around the kvlcc2 tanker at model and full-scale Reynolds numbers, Ocean Eng. 129 (2017) 133–148.
[17] W. Kim, S. Van, D. Kim, Measurement of flows around modern commercial ship models, Exp. Fluids 31 (5) (2001) 567–578.
[18] Z. Shen, D. Wan, et al., Numerical simulation of sphere water entry problem based on VOF and dynamic mesh methods, in: The Twenty-First International Offshore and Polar Engineering Conference, International Society of Offshore and Polar Engineers, 2011.
[19] L. Larsson, F. Stern, M. Visonneau, Numerical Ship Hydrodynamics: An Assessment of the Gothenburg 2010 Workshop, Springer, 2013.
[20] T. Xing, P. Carrica, F. Stern, Computational towing tank procedures for single run curves of resistance and propulsion, J. Fluids Eng. 130 (10) (2008) 101102.
[21] P.M. Carrica, A.M. Castro, F. Stern, Self-propulsion computations using a speed controller and a discretized propeller with dynamic overset grids, J. Mar. Sci. Technol. 15 (4) (2010) 316–330.
[22] H. Yasukawa, Y. Yoshimura, Introduction of mmg standard method for ship maneuvering predictions, J. Mar. Sci. Technol. 20 (1) (2015) 37–52.